HELDA
HELSINGIN YLIOPISTO
HELSINGFORS UNIVERSITET
UNIVERSITY OF HELSINKI

UNIVERSITY OF HELSINKI

https://helda.helsinki.fi

Pt-Decorated TiO2 Materials Supported on Carbon : Increasing Activities and Stabilities toward the ORR by Tuning the Pt Loading

Barbosa, Eduardo C. M.

2019-08

Barbosa , E C M , Parreira , L S , de Freitas , I C , Aveiro , L R , de Oliveira , D C , dos Santos , M C & Camargo , P H C 2019 , ' Pt-Decorated TiO2 Materials Supported on Carbon : Increasing Activities and Stabilities toward the ORR by Tuning the Pt Loading ' , Acs applied energy materials , vol. 2 , no. 8 , pp. 5759-5768 . https://doi.org/10.1021/acsaem.9b00879

http://hdl.handle.net/10138/321548
https://doi.org/10.1021/acsaem.9b00879

acceptedVersion

Downloaded from Helda, University of Helsinki institutional repository.

This is an electronic reprint of the original article.

This reprint may differ from the original in pagination and typographic detail.

Please cite the original version.

Pt-decorated TiO_2 materials supported on carbon: increasing activities and stabilities towards the ORR by tuning the Pt loading

*Eduardo C. M. Barbosa[a, +], Luanna S. Parreira[a, +], Isabel C. de Freitas[a], Luci R. Aveiro[b], Daniela C. de Oliveira[c], Mauro C. dos Santos[b], and Pedro H. C. Camargo[a,d]**

[a] Departamento de Química Fundamental, Instituto de Química, Universidade de São Paulo, Av. Prof. Lineu Prestes, 748, 05508-000 São Paulo, SP, Brazil

[b] Laboratório de Eletroquímica e Materiais Nanostruturados - Centro de Ciências Naturais e Humanas, Universidade Federal do ABC, Rua Santa Adélia, 166, 09210-170, Santo André, SP, Brazil

[c] Centro Nacional de Pesquisa em Energia e Materiais, Laboratório Nacional de Luz Síncrotron, 13083-970, Campinas, SP, Brazil

[d] Department of Chemistry, University of Helsinki, A.I. Virtasen aukio 1, Helsinki, Finland

*Corresponding author: Email: pedro.camargo@helsinki.fi

[+] These authors contributed equally to this article

Abstract

Pt nanoparticles (Pt NPs) supported on carbon have been widely employed as electrocatalysts towards the oxygen reduction kinetics. The development of more efficient electrocatalysts that enable one to reduce or even not require the use of Pt is a central challenge. In addition to the control over Pt NPs physical and chemical features, metal-support interactions can be employed to enhance activities via the generation and exposure of surface-active sites. In this context, we report herein the development of electrocatalysts composed of Pt NPs supported on TiO_2 microspheres, that were subsequently impregnated onto carbon. We have found that by optimizing the loading of Pt at the TiO2 surface, the electrocatalytic activity towards the ORR could be improved compared to the commercial Pt/C (E-TEK) material, even at lower Pt loadings. The enhancement in activities could be assigned to the balance between Pt loading and generation of reactive surface sites, such as adsorbed oxygenated species. Moreover, the utilization of TiO_2 as support enabled improved stabilities relative to Pt/C (E-TEK). We believe that the results described herein may inspire the development of electrocatalysts for the ORR with improved activities and stabilities.

Keywords: Oxygen reduction reaction, electrocatalysis, Pt nanoparticles, TiO_2, metal-support interactions, controlled synthesis

Introduction

The oxygen reduction reaction (ORR) is employed at the cathode in proton exchange membrane (PEM) fuel cells and contributes to the energy production of these devices.[1,2] Due to its sluggish kinetics, the ORR requires electrocatalysts based on platinum nanoparticles (Pt NPs) supported on high surface area materials.[3,4] However, due to the high costs and low abundance of Pt, the reduction in Pt loading or even developing Pt-free electrocatalysts represents an important challenge.[5,6] Recently, significant progress has been achieved in performance through the control over the Pt shape, size, composition (alloys and multimetallic systems), and structure (Pt-based nanostructures with hollow interiors).[3,7] Nevertheless, further understanding of the electrocatalytic enhancements are still required to meet cost/energy demands and enable the widespread application of these devices.[8,9]

In addition to the NPs physical and chemical parameters, the optimization over metal-support interactions can be employed to maximize electrocatalytic performance due to metal-support interactions such as the generation of surface reactive sites.[10–12] In the context of the ORR, most supports are comprised of conductive carbon nanomaterials.[6,13] However, carbon supports usually corrode to form carbon dioxide, leading to the collapse and agglomeration of Pt NPs and thus the loss of activity in the longer term.[14,15] Therefore, the utilization of other supports is promising to improve both the stability and performances. Among the several promising materials as supports, titanium dioxide (TiO_2) is resistant to corrosion, presents a low cost, is commercially available, and several protocols for the

synthesis have been reported.[16,17] However, a major drawback is that the TiO_2 electrical conductivity must be enhanced to be used as a support material. In this case, hybrid materials comprised of TiO_2 and carbon have been proposed. This system combines the attractive features of both materials. Nevertheless, a deeper understanding of the effect of TiO_2 as support over the detected ORR activities and stabilities is required.[16,18]

In this paper, we developed electrocatalysts composed of Pt NPs supported on TiO_2 microspheres, that were subsequently impregnated into conductive carbon (Vulcan) as model systems to investigate the effect of the Pt loading on TiO_2 over the ORR activities and stability. The effect of Pt loading at the TiO_2 surface, as well as the Pt/TiO_2 loading on carbon, was investigated and benchmarked against the commercial Pt/C (E-TEK) material. We found that the loading of Pt and TiO_2 played a central role over the exposure of reactive sites and thus to the ORR activities. This effect could be related to the generation of surface reactive groups, such as adsorbed oxygenated species, as a result of the optimized metal-support interactions.

Experimental

Materials and Instrumentation

$H_2PtCl_6 \cdot 6H_2O$ (Chloroplatinic acid hexahydrate, Sigma-Aldrich), PVP (polyvinylpyrrolidone, Sigma-Aldrich, MW 55 000 g mol^{-1}), EG (ethylene glycol, 99.5%, Synth), C_3H_6O (acetone, 99.5%, Synth), $C_2H_4O_2$ (acetic acid, 99.7%, Vetec), $C_6H_8O_6$ (ascorbic acid, 99.0%, Sigma-Aldrich), $Ti(OBu)_4$ (titanium butoxide, 97%, Sigma-Aldrich), Vulcan XC-72

Carbon (Cabot®), H_2SO_4 (sulfuric acid, 70%, P.A. Synth), Nafion® (5 wt.%, Fluka), and Pt/C E-TEK 10 wt.% were used as received. All chemicals were analytical grade reagents and were used without further purification. Deionized water (18.2 MΩ) was used throughout the experiments.

Scanning electron microscopy (SEM) images were obtained using a JEOL microscope FEG-SEM JSM 6330F operated at 5 kV. The samples were prepared by drop-casting an aqueous suspension of the nanostructures on a Si wafer followed by drying under ambient conditions. Size distribution profile was determined by individually measuring the size of 200 particles from SEM images. Transmission electron microscopy (HRTEM) images were obtained using a Tecnai FEI G20 operated at 200 kV. Samples were prepared by drop casting an alcoholic suspension of each particle in a carbon-coated copper grid followed by drying under ambient conditions.

The X-ray photoelectron spectroscopy (XPS) analyses were performed using a SPECSLAB II (Phoibos-Hsa 3500 150, 9 channeltrons) SPECS spectrometer, with an Al Kα source (E = 1486.6 eV) working at 12 kV, Epass = 40 eV, with 0.2 eV energy step. The synthesized electrocatalysts were kept on stainless steel sample-holders and transported under inert atmosphere into the pre-chamber of the XPS staying under vacuum for 2 hours. The residual pressure in the analysis chamber was of approximately 1×10^{-9} Torr. The binding energies (BE) of Pt 4f, Ti 2p, O 1s, and C 1s spectral peaks were adjusted using the C 1s peak as reference, placed at 284.5 eV, providing accuracy within ± 0.2 eV.

X-ray diffraction (XRD) data were obtained using a Rigaku - Miniflex equipment with CuKα radiation of 1.5406 Å and the diffraction patterns were acquired in the range of 2θ = 10 – 80° with a 1° min–1 scanning speed. Pt atomic percentages were measured by inductively coupled plasma optical emission spectrometry (ICP-OES) using a Spectro Arcos equipment at IQ-USP analytical center facilities. Samples were prepared by digesting them using aqua regia at reflux for 2 hours at 100°C. After digestion, samples were diluted using distilled water.

Synthesis of TiO_2 colloidal spheres

The synthesis followed a previously reported procedure.[19,20] Typically, $Ti(OBu)_4$ (4 mL) were added dropwise to ethylene glycol (90 mL) and kept under vigorous stirring at room temperature for 8 hours. This mixture was then quickly poured into a mixture containing acetone (400 mL), deionized water (5 mL), and acetic acid (2 mL). Subsequently, the mixture was kept under stirring at room temperature for 2 hours followed by aging for 3 more hours. At this stage, titanium glycolate microspheres were formed. They were washed and isolated by successive rounds of centrifugation, removal of the supernatant, and re-suspension in ethanol. In the next step, deionized water (50 mL) was added to the solid material comprising titanium glycolate microspheres, the materials were re-suspended, and this mixture was kept under stirring at 70 °C for 8 hours to produce TiO2 colloidal spheres. This material was washed and isolated by successive rounds of centrifugation, removal of the supernatant, and re-suspension with water and ethanol. The TiO_2 colloidal spheres were then resuspended in deionized water (500 mL).

Synthesis of Pt/TiO_2 via Pt seeded growth

TiO_2 microspheres (12 mg) suspended in deionized water (6 mL) were added to a mixture containing deionized water (12 mL), ascorbic acid (12 mg), and PVP (70 mg). This orange mixture was kept under stirring for 10 minutes at 90 °C and at this point, $PtCl_6^{2-}{}_{(aq)}$ (6 mL, 3.0 mmol L^{-1}) was quickly added to the mixture, which after 10 minutes produced a change in color to black as a result of Pt deposition at the TiO_2 surface. The reaction was allowed to proceed for other 30 minutes at 90°C. This was the first reduction step, the material obtained at this stage was denoted Pt/TiO_2-1, in which the number 1 refers to one Pt deposition step. A second reduction step was performed by adding more $PtCl_6^{2-}{}_{(aq)}$ solution (6 mL, 3.0 mmol L^{-1}) to the reaction mixture obtained at the end of the first reduction step, followed by stirring at 90°C for other 30 min. Similarly, a third reduction step was carried out by adding more $PtCl_6^{2-}{}_{(aq)}$ solution (6 mL, 3.0 mmol L^{-1}) to the reaction mixture obtained at the end of the second reduction step, followed by stirring at 90 ^oC for another 30 min. As described in the first deposition step, the solids that were obtained after the second and third reduction steps were denoted Pt/TiO_2-2 and Pt/TiO_2-3, respectively. These materials were isolated by stopping the reaction at the end of each corresponding reduction step. In all cases, the products were harvested by centrifugation, washed several times with water and ethanol, and re-suspended in water for further use. These samples were dried and weighed for ICP-OES analyses.

Impregnation of Pt/TiO_2-1, Pt/TiO_2-2, and Pt/TiO_2-3 onto carbon Vulcan XC-72

The Pt/TiO_2-1, Pt/TiO_2-2, and Pt/TiO_2-3 materials were impregnated onto a carbon support in order to produce 10% wt. Pt/TiO_2-1/C, Pt/TiO_2-2/C, and Pt/TiO_2-3/C on Vulcan XC-72 Carbon (Cabot®) by a wet impregnation method. Typically, Carbon (50 mg) was used as support for the nanomaterials. The supports were added to aqueous suspensions containing 5 mg of each material and left under vigorous magnetic stirring at 110°C until dry.

Electrochemical studies

The electrochemical experiments were performed at 25°C in an electrochemical three-electrode cell with H_2SO_4 (80 mL, 0.5 mol L^{-1}) as support electrolyte using a potentiostat/galvanostat PGSTAT model 302 N (Autolab®) coupled to a rotating ring-disk electrode accessory (Pine®) and controlled by the Nova 10.1 software. The counter electrode was a platinum rod, while an Ag/AgCl electrode (Analyzer®) was used as reference. The work electrode was a rotating ring-disk electrode consisting of a glassy carbon disk (0.196 cm^2) and platinum ring (0.037 cm^2) with the collection factor of 0.37. After thoroughly characterizing the catalysts, a suspension of each material was prepared in milli-Q water in order to deposit them onto the electrode. An ink was prepared using 1 mg of electrocatalyst and 1 mL of ultrapure water (Milli Q system, 18.2 mΩ cm^{-1}) sonicated for 30 minutes. The glassy carbon disk surface was covered by a drop of 20 uL of the electrocatalytic ink and dried under N_2 flux. Subsequently, 20 µL of a 1:100 solution of Nafion® and ultrapure water were dropped onto

the material, and then further dried under N_2 flux at room temperature. The electrocatalysts were then further characterized regarding their electrocatalytic properties.

For CO stripping measurements, carbon monoxide was adsorbed on a 20 mV polarized electrode, during 5 minutes, immersed in an H_2SO_4 solution (0.5 mol L^{-1}). Subsequently, CO was removed from the electrolyte by purging with N_2 for 25 minutes, and three consecutive cyclic voltammetries were run with a scan rate of 10 mV s^{-1} within the potential range of 0.01 to 1.01 V *versus* RHE reference electrode. The electrochemical surface areas (ESA)[21] for CO stripping were obtained by integrating the area under each CO oxidation peaks in the first voltammetric cycle (Q_{CO}, in mC), these were then divided by the charge needed to oxidize a CO monolayer adsorbed onto a Pt surface (Q_{CO} = 420 µC cm^{-2}). These values were then normalized by the mass of Pt on each electrode and the ECSA was obtained in m^2 g^{-1}.

For the oxygen reduction reaction (ORR), linear scanning voltammograms were collected with a scan rate of 0.01 V s^{-1} in an ultrapure O_2 saturated H_2SO_4 electrolyte (0.5 mol L^{-1}, 30 minutes of O_2 purge) in the potential range between 1.21 and 0.21 V (*vs* RHE) in different rotation speeds (ω) from 100 to 2500 rpm. For experiments performed under light irradiation, a UV LED stick (UVP Pen-Ray (R) Light source) was used. All the analyses were performed in triplicate.

Accelerated stress tests (AST)

In order to study the stability of the electrocatalysts, the most promising catalyst (Pt/TiO_2-2/C) was compared to the commercial material (Pt/C E-TEK) in accelerated stress tests. A typical test was performed in H_2SO_4 (0.5 mol L^{-1}) as support electrolyte. An ORR polarization curve was then collected with a scan rate of 0.01 V s^{-1} in an ultrapure O_2 saturated H_2SO_4 electrolyte (0.5 mol L^{-1}, 30 minutes of O_2 purge) in the potential range between 1.21 and 0.21 V (*vs* RHE) in different rotation speeds (ω) from 100 to 2500 rpm. After performing the ORR, the electrolyte was switched for a fresh one and N_2 was bubbled for 30 minutes before performing the cycles, 1000 cyclic voltammetries were run with a scan rate of 100 mV s^{-1} within the potential range of 0.01 to 1.01 V *versus* RHE. Oxygen was once again bubbled for 30 minutes and ORR was performed in the same conditions as previously established.

Results and discussion

Figure S1A and **B** show SEM and HRTEM images of the TiO_2 colloidal spheres that were employed supports for the Pt/TiO_2 materials. The TiO_2 spheres displayed spherical shape and were 267.8 ± 37.8 nm in diameter. Although they appear to be smooth from SEM images, HRTEM results revealed that they are comprised of TiO_2 nanocrystallites (around 10 nm in size). They were crystallized as anatase according to previously reported XRD and Raman data.[19,22]

The TiO_2 colloidal spheres were employed as seeds for Pt deposition at their surface with controllable sizes and coverage by a facile route based on sequential deposition steps as

depicted in **Figure S2**. This approach employed $PtCl_6^{2-}$ as the Pt precursor, ascorbic acid as a reducing agent, PVP as a stabilizer, water as the solvent, and 90°C as the reaction temperature. The loading and coverage of Pt at the surface could be controlled by performing successive deposition steps, which allows for the understanding of how these parameters affect the electrocatalytic activity of the generated materials towards the ORR. Specifically, three Pt deposition steps were performed, which led to Pt/TiO_2-1, Pt/TiO_2-2, and Pt/TiO_2-3 materials (obtained after one, two, and three Pt deposition steps, respectively).

SEM images for the Pt/TiO_2-1, Pt/TiO_2-2, and Pt/TiO_2-3 materials (**Figure 1A-C**, respectively) indicate the efficient deposition of Pt NPs at the TiO_2 supports displaying a uniform surface dispersion, spherical shape, and uniform sizes. The Pt content and coverage at the TiO_2 surface could be tailored by performing sequential reduction steps. The ICP-OES analyses indicated the presence of 20.1, 31.0, and 38.4 wt.% of Pt in the Pt/TiO_2-1, Pt/TiO_2-2, and Pt/TiO_2-3 samples, respectively. Moreover, Pt NPs diameters calculated from the SEM images corresponded to 11.9 ± 3.0, 16.0 ± 2.2, and 20.1 ± 2.1 nm (histograms on **Figure S3**), respectively. HRTEM images for the Pt/TiO_2-1, Pt/TiO_2-2, and Pt/TiO_2-3 samples (**Figure 1D-F**, respectively) revealed that the individual Pt NPs were comprised of aggregates made up of individual, smaller Pt NPs measuring about 3 nm in size (estimated based on TEM images). While a lower Pt coverage at the TiO_2 surface can be observed for both Pt/TiO_2-1 and Pt/TiO_2-2 samples (**Figure 1D** and **E**), the highest coverage was detected in the Pt/TiO_2-3 material (**Figure 1F**).

After the syntheses, the Pt/TiO_2-1, Pt/TiO_2-2, and Pt/TiO_2-3 samples were incorporated onto Vulcan XC-72 Carbon (Cabot®) by wet impregnation. This led to Pt/TiO_2-1/C, Pt/TiO_2-2/C, and Pt/TiO_2-3/C materials, respectively. In all cases, the Pt/TiO_2 loading corresponded to 10 wt.%, reaching the overall Pt loading of 2.01, 3.10, and 3.84 wt.% for Pt/TiO_2-1/C, Pt/TiO_2-2/C, and Pt/TiO_2-3/C, respectively. **Figure S4** shows the XRD profiles for the Pt/TiO_2-1/C, Pt/TiO_2-2/C, and Pt/TiO_2-3/C materials. The diffractograms show the characteristic reflections assigned to TiO_2 anatase, *fcc* Pt, and carbon. This indicates that our wet impregnation approach was effective for the incorporation of Pt/TiO_2 onto the carbon support.

In order to probe the generation of ORR reactive sites in the Pt/TiO_2-3/C materials as a result of metal-support interactions, the samples were studied by XPS. **Figure 2A-D** shows the Ti 2p, Pt 4f, C 1s, and O 1s core level XPS spectra along with their fitting and deconvoluted curves, obtained for the Pt/TiO_2-1/C, Pt/TiO_2-2/C, and Pt/TiO_2-3/C materials. Data for Vulcan XC-72 carbon is also shown for comparison. The corresponding XPS parameters obtained from the spectra are shown in **Table 1** (for Ti, Pt, and O) and **2** (for C). The Ti 2p spectrum (**Figure 2A**) displayed doublet peaks at 459.4 eV and 465.1 eV assigned to Ti $2p_{3/2}$ and Ti $2p_{1/2}$, respectively. The splitting width between the two peaks was 5.7 eV, indicating the presence of only the Ti^{4+} chemical state.[23] Ti 2p peaks were slightly shifted towards higher binding energies as compared to those in TiO_2, which indicates a change in the Ti chemical environment possibly due to strong interactions with the Carbon support (such as the formation of Ti-O-C bonds).[24]

As shown in **Figure 2B**, the Pt 4f region revealed that the $4f_{7/2}$ and $4f_{5/2}$ spin-orbital components had an asymmetric shape which is typical for Pt^0.[25,26] The peaks located at 71.5 and 74.9 eV can be assigned to Pt $4f_{7/2}$ and Pt $4f_{5/2}$ of Pt^0, respectively. The slight shift towards higher binding energy values compared to literature values (71.0 eV) is attributed to metal-support interaction and to small Pt NPs sizes.[26,27] This positive shift may also suggest meta-support interactions between TiO_2 and Pt. This interaction can modify the electronic properties of Pt by increasing the Pt d-vacancy via electronic donation to Lewis acid centers such as Ti^{x+} at the Pt/TiO_2 interface.[28–30]

Regarding the C 1s region, it was possible to deconvolute the C 1s spectrum into six peaks (**Figure 2C**). The lowest binding energy and dominant peak at about 284.5 eV corresponds to the graphitic carbon phase,[31] while the peak at around 286.0 eV is assigned to hydrocarbons (C-H) from defects on the graphitic structure.[32] Three carbon-oxygen bonding structures for the –C-OH, >C=O and –COOH can also be observed at approximately 287.5, 289.2 and 290.8 eV, respectively. The subpeak located at higher than 292.8 eV is related to $\pi \rightarrow \pi*$ plasmonic excitation.[33] It is noteworthy that it has been established that acidic oxygenated species contribute to the generation of H_2O_2 in the ORR.[34,35] In our case, XPS data indicate that the Pt/TiO_2-2/C sample presented the lowest amount of oxygenated species on the surface (as seen on I_{oxy}/I_c depicted in **Table 2**). Therefore, it can be anticipated that this material would generate the lowest amount of H_2O_2 during the reaction and lead to a higher ORR current density relative to the other samples (Pt/TiO_2-1/C and Pt/TiO_2-3/C).[22]

The O 1s core level peaks for the Pt/TiO_2/C materials are shown in **Figure 2D**. The O 1s peaks could be deconvoluted in three peaks. The first component (O_I) centered at 531 eV was attributed to the lattice oxygen in the oxides and C=O functional groups. The second and dominant component (O_{II}) located at 533 eV was attributed to chemisorbed oxygen species (such as OH^-) and functional C-O groups. The last component (O_{III}) with BE around 536 eV were characteristic of adsorbed water.[24,36]

After probing the metal-support interactions and generation of reactive surface species by XPS, we investigated their electroactive areas by CO stripping as described in **Figure S5**. The Pt/TiO_2/C materials presented lower onset potential for carbon monoxide oxidation when compared to commercial Pt/C E-TEK, a behavior related to the interaction between Pt and TiO_2. This interaction (as suggested by XPS data) decreases the adsorption of CO at the metal surface facilitating the oxidation.[37] A main current density peak was detected between 0.76 and 0.80 V *vs* RHE (Reversible Hydrogen Electrode) for all materials, which is assigned to the CO oxidation on the Pt sites interacting with sp^3 disordered carbon.[1,38] In addition, a shoulder at lower potentials was observed (0.46 V *vs* RHE) for the Pt/TiO_2-3/C, which can be assigned to the partial agglomeration of Pt NPs on the TiO_2 surface caused by the higher Pt coverage in this material.[39] The ESA (electrochemical surface area) and ECSA (electrochemical active surface area) of the materials calculated from the CO-stripping experiments are depicted in **Table S1**.[40] It can be observed that the ECSA increased with the Pt loadings, corresponding to 2.41, 9.78, and 25.2 m^2g^{-1} for Pt/TiO_2-1/C, Pt/TiO_2-2/C, and Pt/TiO_2-3/C materials, respectively. Here, the Pt content in the samples increases in the order of Pt/TiO_2-

3/C > Pt/TiO_2-2/C > Pt/TiO_2-1/C (samples 1, 2, and 3 were prepared after successive Pt deposition steps). Therefore, the Pt ECSA increases with the Pt loading in the Pt/TiO2/C samples. However, it is important to note that these ECSA values were significantly lower as compared to Pt/C E-TEK (68.2 m^2g^{-1}). This is probably due to the aggregation of the Pt NPs on the TiO_2 surface as observed by HRTEM.

Figure 3A-D depicts the linear sweep voltammetries (LSV) for the Pt/TiO_2-1/C (**Figure 3A**), Pt/TiO_2-2/C (**Figure 3B**), and Pt/TiO_2-3/C (**Figure 3C**) and Pt/C E-TEK (**Figure 3D**) materials towards the ORR performed in O_2 saturated H_2SO_4 (0.5 mol L^{-1}) at different rotation rates (from 100 rpm to 2500 rpm as indicated by the colors in the inset, **Figure 3A**). The detected currents were normalized by the geometric surface areas of the electrodes (0.196 cm^2 for the disk and 0.037 cm^2 for the ring) and presented as current densities. **Figure 3E-H** depicts the disk currents for the ORR, respectively, using each electrocatalyst shown in **Figure 3A-D**. These results show an increase in ring current density values (**Figure 3A-D**) on potentials lower than 0.80 V *vs* RHE, which indicates the conversion of O_2 onto H_2O_2 as detected by its oxidation on the ring electrode.[41–44] However, the disk current density (**Figure 3E-H**) is lowered in potentials below 0.80 V, which indicates the formation of H_2O.

Additionally, LSV of the ORR on the disk indicates a mixed kinetic-diffusion control region between potentials of 0.90 V and 0.60 V. This region is narrower under low rotations and becomes larger at higher rotations. The region between 0.60 V and lower potentials is assigned to the diffusional control region. This behavior is normally seen for Pt-based

electrocatalysts.[45] The disk's limiting current density increased gradually with the rotation rate, as expected for a diffusional-controlled reaction.[46]

The water production efficiency (and consequently, the number of exchanged electrons per O_2 molecule) was calculated using the ring current densities using **Equation 1** and **2:** [47]

$$p\,(H_2O) = 2 \times \frac{\frac{i_r}{N_c}}{i_d + \frac{i_r}{N_c}} \quad \textbf{(1)}$$

$$n = 4 \times \frac{i_d}{i_d + \frac{i_r}{N_c}} \quad \textbf{(2)}$$

where N_c is the collection factor (experimentally determined as N_c= 0.37), i_d is the disk current, i_r is the ring current. These values are listed in **Table 3**. A small amount of electrogenerated hydrogen peroxide is observed from the ring current densities presented in **Figure 3**. When comparing the limiting current densities of the ring and disk on the commercial material, we can see that the ring current density is about 2500 times lower than the disk, confirming that these electrodes produce mainly water (low hydrogen peroxide current). Hence, the number of electrons is closer to 4.

Considering Pt as the standard electrocatalytic metal for ORR via 4 electrons and that the experimental values obtained for Pt/C E-TEK were close to the theoretical ones (3.98 electrons 98.8% water), the number of electron and water percentages were compared in the diffusional region for all materials. These values become lower when the Pt loading on TiO_2 increases, which could be assigned to the preferential 4-electron mechanism of Pt for the ORR.

From the ring curves (**Figure 3E-H**), two behavior changes are also noticed at 0.70 V and 0.30 V (*vs* RHE), which were more significantly seen on the Pt/TiO_2-1/C material. It is

suggested that the ORR on the disk, and consequently the oxidation of H_2O_2 on the ring, occur as a function of the applied potential. Our results suggest that there are probably two mechanisms of formation of hydrogen peroxide, one at lower overpotentials and one at higher overpotentials. In order to better understand the reaction mechanism, Tafel curves were plotted from RDE data by the mass-transport correction of the current density measured for rotating disk electrodes and are presented in **Figure 4** according to **Equation 3**:

$$j_k = \frac{j_d * j}{j_d - j} \quad (\mathbf{3})$$

where j is the experimentally measured current density, j_d is the obtained diffusion-limited current density, and j_k is the kinetic current density without the mass-transport effect. These values were calculated using the current density normalized by geometric area. The Tafel curves for the electrocatalysts presented two different regions, a behavior which is expected for Pt-based catalysts. At lower overpotentials, all the electrocatalysts presented slopes between -70 and -90 mV dec^{-1}, reaching the highest value on Pt/TiO_2-1/C (86.5 mV dec^{-1}), which indicates that the mechanism of oxygen adsorption is similar to bulk Pt at 1.06 - 0.96 V (*vs* RHE) potentials.[14,18,48] However, at higher overpotentials, there is an increase on the slope with the decrease in module of the Pt amount on the electrocatalyst from -124.7 mV dec^{-1} (Pt/C E-TEK) to -135.2 mV dec^{-1} (Pt/TiO_2-1/C).[49] This observation indicates that the current densities are related to the oxygen adsorption energy on the electrocatalyst surface and that the first electron transfer is the determining step of the ORR.[16] These slope values were also

observed for other TiO_2-based electrocatalysts.[14,16,49] When comparing the Tafel plot for all the materials employed in this work, we can notice that the Pt/TiO_2-2/C material presented a profile very similar to the Pt/C E-TEK material, even though it presents lower Pt content.

Previous studies have shown that high slopes on the Tafel plot are normally associated with the rate determining step of the ORR, the O_2 adsorption onto the metal.[50] Tafel slopes normally increase on materials with lower Pt contents, which indicates that the mechanism tends to involve a 2-electron reaction. This was also observed for our materials when compared to the commercial Pt/C.[51] According to Shinagawa *et al.*[50], the mechanism of the ORR is based on three different surface covering species, which are responsible for the slopes on the Tafel plot. At lower overpotentials, the theoretical slopes can vary from 40 to 120 mV dec^{-1} depending on the adsorbed species contributing to the rate determining step. As the slope lowers, it indicates there are more MOO^- and MOOH species contributing to the rate-determining step of the reaction, while at higher slopes the rate determining step is governed by MOO adsorption. Hence, while the reaction on the Pt/C E-TEK catalyst is determined initially by MOO groups, the reaction also depended on the generation of MOO^- and MOOH groups in the Pt/TiO_2/C materials. On the other hand, at higher overpotentials, the Tafel slope is normally ≥ 120 mV dec^{-1}, which indicates that the MOO and MOOH species are converting into MOO^- species. Thus, the detected higher slopes show that the conversion starts in lower overpotentials and/or these catalysts already present a high number of MOO^- species on their surface. This figure also shows that while the change in slope occurred at 0.775 V for the Pt/C E-TEK material, this change was only seen at higher overpotentials for

the Pt/TiO_2/C materials. Moreover, based on DFT simulations,[52] a strong interaction between Pt and TiO_2 is presumed due to the overlapping of the TiO_2 bonding orbitals with the Pt d-orbital. These calculations also indicate a strong interaction between Ti and Pt that could result in a negative overall net charge in this structure which could strengthen the Pt-O_{ads} bond. Therefore, the desorption process could become slow in the high overpotential region, thus increasing the Tafel plot as observed in our data.

In order to better compare the relative ORR electrocatalytic activity of our materials, the ORR linear scanning voltammetries at 1600 rpm rotation rate were plotted as shown in **Figure 5A.** In addition, the electrocatalytic activity normalized by geometric mass (left-hand side) and Pt mass on the electrode (right-hand side) at 0.80 V (*vs* RHE) are shown in **Figure 5B**. The Pt/C E-TEK material presented a more positive onset potential for the ORR (0.89 V) followed by Pt/TiO_2-2/C (0.88 V), Pt/TiO_2-3/C (0.84 V), and Pt/TiO_2-1/C (0.82 V). Here, it is important to note that the Pt/TiO_2/C materials have less than half Pt content in their composition compared to the commercial electrocatalyst. In agreement with the ORR onset potential, the number of transferred electrons follows the trend: Pt/C E-TEK > Pt/TiO_2-2/C > Pt/TiO_2-3/C > Pt/TiO_2-1/C, indicating that the reaction is kinetically favorable in this order.

Interestingly, even though the electrodes covered by Pt/TiO_2/C hybrids have Pt loadings that range from threefold to fivefold lower than the one containing Pt/C E-TEK, they still present similar limiting diffusional current densities.[53] This led to much higher activities when the data is normalized by Pt mass in **Figure 5B**. Specifically, the Pt/TiO_2-2/C material displayed a starting reduction potential close to Pt/C E-TEK (0.89 V and 0.88 V *vs* RHE,

respectively). The higher activity of the Pt/TiO_2-2/C material could be attributed to its lowest number of acidic oxygenated species at the surface as determined by XPS. These sites decrease the H_2O_2 formation thus enhancing the water production and the current on the disk relative to the other materials[22]. This material also displays less Pt NPs aggregation at the surface as compared to Pt/TiO_2-3/C (**Figure 1**). It is noteworthy that the Pt/TiO_2-1/C sample presented the highest H_2O_2 production, which can also be attributed to the higher exposure of anatase TiO_2 at the surface as a result of lower Pt coverage.[22,54]

Our data indicate that the control over the Pt NPs coverage at the TiO_2 surface significantly influences their electrocatalytic activities towards the ORR. In this case, rather than an increase in activity with the Pt loading, a volcano-type relationship was observed, in which the sample produced by two Pt deposition steps (Pt/TiO_2-2/C) displayed the highest activities due to the equilibrium between optimum Pt loading/surface coverage and the presence of surface reactive sites as enabled by metal-support interactions.

We also evaluated the stability of the Pt/TiO_2-2/C material relative to Pt/C E-TEK by performing accelerated stress tests (AST) as shown in **Figure 6**. The initial and final ORR polarization curves are depicted as solid and dashed traces, respectively, in **Figure 6A**. The AST curves for the Pt/C E-TEK and Pt/TiO_2-2/C are shown in black and red, respectively. It can be observed that a decrease in activity was detected for both materials after the tests. However, when comparing their half-wave potential before and after the AST, $E_{1/2}$, (**Figure 6B)**, a more significant decrease is detected for Pt/C E-TEK, from 0.747 to 0.646 V *vs* RHE compared to Pt/TiO_2-2/C, which corresponded from 0.727 to 0.697 V *vs* RHE. When

comparing half-wave potentials, shifts to smaller regions indicate an activity loss, thus, since for the commercial materials the shift is higher (approximately 0.31 V *vs* RHE) when compared to Pt/TiO_2-2/C (approximately 0.24 V *vs* RHE). Moreover, after the AST, the number of electrons involved in the reactions and water percentages lowered for both materials, as seen in **Table S2**. While the mean electron number was of 3.94 and 3.92 on the Pt/TiO_2-2/C and Pt/C E-TEK, they produced 97.1 and 96.1% of water, respectively. This further shows the low loss of overall activity of Pt/TiO_2-2/C compared to the Pt/C E-TEK.

In addition to metal-support interactions, the utilization of TiO_2 as support also enables the harvesting of its photocatalytic properties to further improve activities. Therefore, the influence of UV irradiation on the electrocatalytic activity of the Pt/TiO_2-2/C electrocatalyst was also evaluated. The effect of light irradiation was probed in chronoamperometry experiments performed at 0.51 V (*vs* RHE) as shown in **Figure S6A** and the activity towards the ORR by linear scanning voltammogram as shown in **Figure S6B** (rotation rate of 1600 rpm in O_2 saturated 0.5 mol L^{-1} H_2SO_4 solution). Here, the activity under UV excitation was compared with its activity in the absence of UV excitation. **Figure S6A** shows a chronoamperometric assay while applying to the electrode UV light pulses of about 150 seconds. It was observed that under UV light excitation the current density increased in about 4 mA cm^{-2} due to the light excitation. The voltammograms on **Figure S6B** revealed a slight shift to more positive potentials (~30 mV) and an increase of 11.3% on the limiting diffusion current density under UV-excitation. This indicates that the utilization that TiO_2 based electrocatalysts and UV light excitation can be employed to further improve the

electrocatalytic activities towards the ORR. It is anticipated that further optimizations can lead to further improvements both in the photoelectrocatalytic activities and in the use of visible light (instead of UV) by TiO_2 doping or use Au NPs (harvesting of plasmonic effects).

Conclusions

We investigated herein how Pt surface coverage in hybrid materials comprised of Pt NPs supported on TiO_2 colloidal spheres (Pt/TiO_2) influence their electrocatalytic activities towards the ORR. It was demonstrated that, by employing TiO_2 colloidal spheres as physical templates, the uniform deposition of monodisperse and spherical Pt NPs ~3 nm could be achieved. The Pt coverage could be tuned as a function of the deposition steps. After incorporating the Pt/TiO_2 materials into Vulcan XC72 Carbon (to produce $Pt/TiO_2/C$ materials), the electrocatalytic activities towards the ORR as well as the reaction and enhancement mechanisms were investigated. Our results demonstrated that the control over the Pt coverage at the surface plays a pivotal role over the optimization of activities, in which a relationship among Pt content at the TiO_2 surface, the generation of surface reactive sites as a result of metal-support interactions, and ORR performance were unraveled. More specifically, the material produced from two Pt deposition steps displayed the highest activity, which was also superior as compared to commercial Pt/C E-TEK even at lower Pt loadings (between 2.0 and 4.0 wt.% of Pt on the final material). The variations in catalytic activity could be explained by the presence and concentration of surface reactive groups, such as adsorbed

oxygenated species as a function of the Pt coverage. Moreover, the presence of TiO_2 as support enabled increased stability relative to PT/C ETEK. We believe that improvements on the $Pt/TiO_2/C$ interface may allow for the reduction on the voltage loss relative to Pt/C systems and thus further optimizations in performance. These results illustrate that the understanding of the electrocatalytic enhancement mechanism together with the controlled synthesis of Pt-based nanomaterials can lead to tailored surface properties and electrocatalytic activities.

Supporting Information. SEM and HRTEM images, schematics of the synthesis, histograms of size distribution, DRX patterns, CO-stripping and CVs, photoelectrocatalytic experiments, ESA and ESCA values, and RRDE data obtained after the AST tests.

Acknowledgments

This work was supported by FAPESP (grant numbers 2015/21366-9, 2015/26308-7, 2017/21846-6) and the Serrapilheira Institute (Grant Serra-1709-16900). This study was financed in part by the Coordenação de Aperfeiçoamento de Pessoal de Nível Superior – Brazil (CAPES) – Finance Code 001. P.H.C.C and M.C.S. thank the CNPq for the research fellowships. E.C.M.B. and L. S. P. thanks FAPESP for the fellowship (grant numbers 2015/11452-5 and 2016/00819-8, respectively). We also thank the Brazilian Synchrotron Light Laboratory (LNLS, CNPEM) for XPS analysis.

References

(1) Estudillo-Wong, L. A.; Luo, Y.; Díaz-Real, J. A.; Alonso-Vante, N. Enhanced Oxygen Reduction Reaction Stability on Platinum Nanoparticles Photo-Deposited onto Oxide-Carbon Composites. *Appl. Catal. B Environ.* **2016**, *187*, 291–300. https://doi.org/10.1016/j.apcatb.2016.01.030.

(2) ten Elshof, J. E.; Yuan, H.; Gonzalez Rodriguez, P. Two-Dimensional Metal Oxide and Metal Hydroxide Nanosheets: Synthesis, Controlled Assembly and Applications in Energy Conversion and Storage. *Adv. Energy Mater.* **2016**, *6* (23), 1600355. https://doi.org/10.1002/aenm.201600355.

(3) Mistry, H.; Varela, A. S.; Kühl, S.; Strasser, P.; Cuenya, B. R. Nanostructured Electrocatalysts with Tunable Activity and Selectivity. *Nat. Rev. Mater.* **2016**, 16009. https://doi.org/10.1038/natrevmats.2016.9.

(4) Kleijn, S. E. F.; Lai, S. C. S.; Koper, M. T. M.; Unwin, P. R. Electrochemistry of Nanoparticles. *Angew. Chem. Int. Ed.* **2014**, *53* (14), 3558–3586. https://doi.org/10.1002/anie.201306828.

(5) Cheng, X.; Li, Y.; Zheng, L.; Yan, Y.; Zhang, Y.; Chen, G.; Sun, S.; Zhang, J. Highly Active, Stable Oxidized Platinum Clusters as Electrocatalysts for the Hydrogen Evolution Reaction. *Energy Environ. Sci.* **2017**, *10* (11), 2450–2458. https://doi.org/10.1039/C7EE02537H.

(6) Shao, M.; Chang, Q.; Dodelet, J.-P.; Chenitz, R. Recent Advances in Electrocatalysts for

Oxygen Reduction Reaction. *Chem. Rev.* **2016**, *116* (6), 3594–3657. https://doi.org/10.1021/acs.chemrev.5b00462.

(7) Li, Y.; Hart, J. L.; Taheri, M. L.; Snyder, J. D. Morphological Instability in Topologically Complex, Three-Dimensional Electrocatalytic Nanostructures. *ACS Catal.* **2017**, *7* (11), 7995–8005. https://doi.org/10.1021/acscatal.7b02398.

(8) Huang, Z. F.; Wang, J.; Peng, Y.; Jung, C. Y.; Fisher, A.; Wang, X. Design of Efficient Bifunctional Oxygen Reduction/Evolution Electrocatalyst: Recent Advances and Perspectives. *Adv. Energy Mater.* **2017**, *1700544*, 1–21. https://doi.org/10.1002/aenm.201700544.

(9) Liu, J.; Jiao, M.; Lu, L.; Barkholtz, H. M.; Li, Y.; Wang, Y.; Jiang, L.; Wu, Z.; Liu, D.; Zhuang, L.; Ma, C.; Zeng, J.; Zhang, B.; Su, D.; Song, P.; Xing, W.; Xu, W.; Wang, Y.; Jiang, Z.; Sun, G. High Performance Platinum Single Atom Electrocatalyst for Oxygen Reduction Reaction. *Nat. Commun.* **2017**, *8* (1), 15938. https://doi.org/10.1038/ncomms15938.

(10) Matsubu, J. C.; Zhang, S.; DeRita, L.; Marinkovic, N. S.; Chen, J. G.; Graham, G. W.; Pan, X.; Christopher, P. Adsorbate-Mediated Strong Metal–support Interactions in Oxide-Supported Rh Catalysts. *Nat. Chem.* **2016**, *9* (2), 120–127. https://doi.org/10.1038/nchem.2607.

(11) Xu, M.; He, S.; Chen, H.; Cui, G.; Zheng, L.; Wang, B.; Wei, M. TiO 2– x -Modified Ni Nanocatalyst with Tunable Metal–Support Interaction for Water–Gas Shift Reaction. *ACS Catal.* **2017**, *7* (11), 7600–7609. https://doi.org/10.1021/acscatal.7b01951.

(12) Cao, M.; Tang, Z.; Liu, Q.; Xu, Y.; Chen, M.; Lin, H.; Li, Y.; Gross, E.; Zhang, Q. The Synergy between Metal Facet and Oxide Support Facet for Enhanced Catalytic Performance: The Case of Pd–TiO 2. *Nano Lett.* **2016**, *16* (8), 5298–5302. https://doi.org/10.1021/acs.nanolett.6b02662.

(13) El-Sawy, A. M.; Mosa, I. M.; Su, D.; Guild, C. J.; Khalid, S.; Joesten, R.; Rusling, J. F.; Suib, S. L. Controlling the Active Sites of Sulfur-Doped Carbon Nanotube-Graphene Nanolobes for Highly Efficient Oxygen Evolution and Reduction Catalysis. *Adv. Energy Mater.* **2016**, *6* (5), 1–12. https://doi.org/10.1002/aenm.201501966.

(14) Ruiz-Camacho, B.; Valenzuela, M. A.; González-Huerta, R. G.; Suarez-Alcantara, K.; Canton, S. E.; Pola-Albores, F. Electrochemical and XAS Investigation of Oxygen Reduction Reaction on Pt-TiO2-C Catalysts. *Int. J. Hydrogen Energy* **2013**, *38* (28), 12648–12656. https://doi.org/10.1016/j.ijhydene.2013.01.002.

(15) Riese, A.; Banham, D.; Ye, S.; Sun, X. Accelerated Stress Testing by Rotating Disk Electrode for Carbon Corrosion in Fuel Cell Catalyst Supports. *J. Electrochem. Soc.* **2015**, *162* (7), F783–F788. https://doi.org/10.1149/2.0911507jes.

(16) Kim, J. H.; Kwon, G.; Lim, H.; Zhu, C.; You, H.; Kim, Y. T. Effects of Transition Metal Doping in Pt/M-TiO2 (M = V, Cr, and Nb) on Oxygen Reduction Reaction Activity. *J. Power Sources* **2016**, *320*, 188–195. https://doi.org/10.1016/j.jpowsour.2016.04.019.

(17) Jia, C.; Yang, P.; Chen, H.-S.; Wang, J. Template-Free Synthesis of Mesoporous Anatase Titania Hollow Spheres and Their Enhanced Photocatalysis. *CrystEngComm* **2015**, *17* (15), 2940–2948. https://doi.org/10.1039/C4CE02358G.

(18) Ruiz Camacho, B.; Morais, C.; Valenzuela, M. A.; Alonso-Vante, N. Enhancing Oxygen Reduction Reaction Activity and Stability of Platinum via Oxide-Carbon Composites. *Catal. Today* **2013**, *202* (1), 36–43. https://doi.org/10.1016/j.cattod.2012.03.033.

(19) Damato, T. C.; de Oliveira, C. C. S.; Ando, R. A.; Camargo, P. H. C. A Facile Approach to TiO2 Colloidal Spheres Decorated with Au Nanoparticles Displaying Well-Defined Sizes and Uniform Dispersion. *Langmuir* **2013**, *29* (5), 1642–1649.

(20) Cheng, Y.; Guo, J.; Liu, X.; Sun, A.; Xu, G.; Cui, P. Preparation of Uniform Titania Microspheres with Good Electrorheological Performance and Their Size Effect. *J. Mater. Chem.* **2011**, *21* (13), 5051. https://doi.org/10.1039/c0jm03378b.

(21) Nassr, A. B. A. A.; Sinev, I.; Grünert, W.; Bron, M. PtNi Supported on Oxygen Functionalized Carbon Nanotubes: In Depth Structural Characterization and Activity for Methanol Electrooxidation. *Appl. Catal. B Environ.* **2013**, *142–143*, 849–860. https://doi.org/10.1016/j.apcatb.2013.06.013.

(22) dos Reis, F. V. E.; Antonin, V. S.; Hammer, P.; Santos, M. C.; Camargo, P. H. C. Carbon-Supported TiO2–Au Hybrids as Catalysts for the Electrogeneration of Hydrogen Peroxide: Investigating the Effect of TiO2 Shape. *J. Catal.* **2015**, *326*, 100–106.

(23) Liu, C.; Tong, R.; Xu, Z.; Kuang, Q.; Xie, Z.; Zheng, L. Efficiently Enhancing the Photocatalytic Activity of Faceted TiO_2 Nanocrystals by Selectively Loading α-Fe_2O_3 and Pt Co-Catalysts. *RSC Adv.* **2016**, *6* (35), 29794–29801. https://doi.org/10.1039/C6RA04552A.

(24) Wang, P.; Zhan, S.; Xia, Y.; Ma, S.; Zhou, Q.; Li, Y. The Fundamental Role and

Mechanism of Reduced Graphene Oxide in RGO/Pt-TiO2 Nanocomposite for High-Performance Photocatalytic Water Splitting. *Appl. Catal. B Environ.* **2017**, *207*, 335–346. https://doi.org/10.1016/j.apcatb.2017.02.031.

(25) Lian, Z.; Wang, W.; Li, G.; Tian, F.; Schanze, K. S.; Li, H. Pt-Enhanced Mesoporous Ti3+/TiO2 with Rapid Bulk to Surface Electron Transfer for Photocatalytic Hydrogen Evolution. *ACS Appl. Mater. Interfaces* **2017**, *9* (20), 16959–16966. https://doi.org/10.1021/acsami.6b11494.

(26) Dablemont, C.; Lang, P.; Mangeney, C.; Piquemal, J. Y.; Petkov, V.; Herbst, F.; Viau, G. FTIR and XPS Study of Pt Nanoparticle Functionalization and Interaction with Alumina. *Langmuir* **2008**, *24* (11), 5832–5841. https://doi.org/10.1021/la7028643.

(27) Kobayashi, H.; Teranishi, M.; Negishi, R.; Naya, S.; Tada, H. Reaction Mechanism of the Multiple-Electron Oxygen Reduction Reaction on the Surfaces of Gold and Platinum Nanoparticles Loaded on Titanium(IV) Oxide. *J. Phys. Chem. Lett.* **2016**, *7* (24), 5002–5007. https://doi.org/10.1021/acs.jpclett.6b02026.

(28) Bedolla-Valdez, Z. I.; Verde-Gómez, Y.; Valenzuela-Muñiz, A. M.; Gochi-Ponce, Y.; Oropeza-Guzmán, M. T.; Berhault, G.; Alonso-Núñez, G. Sonochemical Synthesis and Characterization of Pt/CNT, Pt/TiO2, and Pt/CNT/TiO2 Electrocatalysts for Methanol Electro-Oxidation. *Electrochim. Acta* **2015**, *186*, 76–84. https://doi.org/10.1016/j.electacta.2015.10.084.

(29) Xia, B. Y.; Wang, B.; Wu, H. Bin; Liu, Z.; Wang, X.; Lou, X. W. Sandwich-Structured TiO2–Pt–graphene Ternary Hybrid Electrocatalysts with High Efficiency and Stability.

J. Mater. Chem. **2012**, *22* (32), 16499. https://doi.org/10.1039/c2jm32816j.

(30) Qin, Y.-H.; Li, Y.; Lv, R.-L.; Wang, T.-L.; Wang, W.-G.; Wang, C.-W. Enhanced Methanol Oxidation Activity and Stability of Pt Particles Anchored on Carbon-Doped TiO2 Nanocoating Support. *J. Power Sources* **2015**, *278*, 639–644. https://doi.org/10.1016/j.jpowsour.2014.12.096.

(31) Wu, G.; Hu, Y.; Liu, Y.; Zhao, J.; Chen, X.; Whoehling, V.; Plesse, C.; Nguyen, G. T. M.; Vidal, F.; Chen, W. Graphitic Carbon Nitride Nanosheet Electrode-Based High-Performance Ionic Actuator. *Nat. Commun.* **2015**, *6*, 7258. https://doi.org/10.1038/ncomms8258.

(32) Zhou, J.-H.; Sui, Z.-J.; Zhu, J.; Li, P.; Chen, D.; Dai, Y.-C.; Yuan, W.-K. Characterization of Surface Oxygen Complexes on Carbon Nanofibers by TPD, XPS and FT-IR. *Carbon N. Y.* **2007**, *45* (4), 785–796. https://doi.org/10.1016/j.carbon.2006.11.019.

(33) Ganguly, A.; Sharma, S.; Papakonstantinou, P.; Hamilton, J. Probing the Thermal Deoxygenation of Graphene Oxide Using High-Resolution In Situ X-Ray-Based Spectroscopies. *J. Phys. Chem. C* **2011**, *115* (34), 17009–17019. https://doi.org/10.1021/jp203741y.

(34) Assumpção, M. H. M. T.; De Souza, R. F. B.; Rascio, D. C.; Silva, J. C. M.; Calegaro, M. L.; Gaubeur, I.; Paixão, T. R. L. C.; Hammer, P.; Lanza, M. R. V; Santos, M. C. A Comparative Study of the Electrogeneration of Hydrogen Peroxide Using Vulcan and Printex Carbon Supports. *Carbon N. Y.* **2011**, *49* (8), 2842–2851. https://doi.org/10.1016/j.carbon.2011.03.014.

(35) Assumpção, M. H. M. T.; Moraes, A.; De Souza, R. F. B.; Calegaro, M. L.; Lanza, M. R. V.; Leite, E. R.; Cordeiro, M. A. L.; Hammer, P.; Santos, M. C. Influence of the Preparation Method and the Support on H2O2 Electrogeneration Using Cerium Oxide Nanoparticles. *Electrochim. Acta* **2013**, *111*, 339–343. https://doi.org/10.1016/j.electacta.2013.07.187.

(36) Salgado, J. R. C.; Paganin, V. A.; Gonzalez, E. R.; Montemor, M. F.; Tacchini, I.; Ansón, A.; Salvador, M. A.; Ferreira, P.; Figueiredo, F. M. L.; Ferreira, M. G. S. Characterization and Performance Evaluation of Pt-Ru Electrocatalysts Supported on Different Carbon Materials for Direct Methanol Fuel Cells. *Int. J. Hydrogen Energy* **2013**, *38* (2), 910–920. https://doi.org/10.1016/j.ijhydene.2012.10.079.

(37) Lewera, A.; Timperman, L.; Roguska, A.; Alonso-Vante, N. Metal–Support Interactions between Nanosized Pt and Metal Oxides (WO 3 and TiO 2) Studied Using X-Ray Photoelectron Spectroscopy. *J. Phys. Chem. C* **2011**, *115* (41), 20153–20159. https://doi.org/10.1021/jp2068446.

(38) Ma, J.; Habrioux, A.; Morais, C.; Lewera, A.; Vogel, W.; Verde-Gómez, Y.; Ramos-Sanchez, G.; Balbuena, P. B.; Alonso-Vante, N. Spectroelectrochemical Probing of the Strong Interaction between Platinum Nanoparticles and Graphitic Domains of Carbon. *ACS Catal.* **2013**, *3* (9), 1940–1950. https://doi.org/10.1021/cs4003222.

(39) López-Cudero, A.; Solla-Gullón, J.; Herrero, E.; Aldaz, A.; Feliu, J. M. CO Electrooxidation on Carbon Supported Platinum Nanoparticles: Effect of Aggregation. *J. Electroanal. Chem.* **2010**, *644* (2), 117–126.

https://doi.org/10.1016/j.jelechem.2009.06.016.

(40) Zheng, Y.; Chen, H.; Dai, Y.; Zhang, N.; Zhao, W.; Wang, S.; Lou, Y.; Li, Y.; Sun, Y. Preparation and Characterization of Pt/TiO2 Nanofibers Catalysts for Methanol Electro-Oxidation. *Electrochim. Acta* **2015**, *178*, 74–79. https://doi.org/10.1016/j.electacta.2015.07.177.

(41) Lima, F. H. B.; Lizcano-Valbuena, W. H.; Teixeira-Neto, E.; Nart, F. C.; Gonzalez, E. R.; Ticianelli, E. A. Pt-Co/C Nanoparticles as Electrocatalysts for Oxygen Reduction in H2SO4 and H2SO4/CH3OH Electrolytes. *Electrochim. Acta* **2006**, *52* (2), 385–393. https://doi.org/10.1016/j.electacta.2006.05.019.

(42) Ruiz-Camacho, B.; Martínez-Álvarez, O.; Rodríguez-Santoyo, H. H.; Granados-Alejo, V. Pt/C and Pt/TiO2–C Electrocatalysts Prepared by Chemical Vapor Deposition with High Tolerance to Alcohols in Oxygen Reduction Reaction. *J. Electroanal. Chem.* **2014**, *725*, 19–24. https://doi.org/10.1016/j.jelechem.2014.04.019.

(43) Ferrero, G. A.; Preuss, K.; Marinovic, A.; Jorge, A. B.; Mansor, N.; Brett, D. J. L.; Fuertes, A. B.; Sevilla, M.; Titirici, M.-M. Fe–N-Doped Carbon Capsules with Outstanding Electrochemical Performance and Stability for the Oxygen Reduction Reaction in Both Acid and Alkaline Conditions. *ACS Nano* **2016**, *10* (6), 5922–5932. https://doi.org/10.1021/acsnano.6b01247.

(44) Shih, Y.-H.; Sagar, G. V.; Lin, S. D. Effect of Electrode Pt Loading on the Oxygen Reduction Reaction Evaluated by Rotating Disk Electrode and Its Implication on the Reaction Kinetics. *J. Phys. Chem. C* **2008**, *112* (1), 123–130.

https://doi.org/10.1021/jp071807h.

(45) Santos, L. G. R. A.; Freitas, K. S.; Ticianelli, E. A. Heat Treatment Effect of Pt–V/C and Pt/C on the Kinetics of the Oxygen Reduction Reaction in Acid Media. *Electrochim. Acta* **2009**, *54* (22), 5246–5251. https://doi.org/10.1016/j.electacta.2009.03.078.

(46) Demarconnay, L.; Coutanceau, C.; Léger, J.-M. Study of the Oxygen Electroreduction at Nanostructured PtBi Catalysts in Alkaline Medium. *Electrochim. Acta* **2008**, *53* (8), 3232–3241. https://doi.org/10.1016/j.electacta.2007.07.006.

(47) Zhou, R.; Zheng, Y.; Jaroniec, M.; Qiao, S.-Z. Determination of the Electron Transfer Number for the Oxygen Reduction Reaction: From Theory to Experiment. *ACS Catal.* **2016**, *6* (7), 4720–4728. https://doi.org/10.1021/acscatal.6b01581.

(48) Tiido, K.; Alexeyeva, N.; Couillard, M.; Bock, C.; MacDougall, B. R.; Tammeveski, K. Graphene-TiO2 Composite Supported Pt Electrocatalyst for Oxygen Reduction Reaction. *Electrochim. Acta* **2013**, *107*, 509–517. https://doi.org/10.1016/j.electacta.2013.05.155.

(49) Tammeveski, K. The Reduction of Oxygen on Pt-TiO2 Coated Ti Electrodes in Alkaline Solution. *J. Electrochem. Soc.* **1999**, *146* (2), 669. https://doi.org/10.1149/1.1391660.

(50) Shinagawa, T.; Garcia-Esparza, A. T.; Takanabe, K. Insight on Tafel Slopes from a Microkinetic Analysis of Aqueous Electrocatalysis for Energy Conversion. *Sci. Rep.* **2015**, *5* (August), 1–21. https://doi.org/10.1038/srep13801.

(51) Elezovic, N. R.; Babic, B. M.; Radmilovic, V. R.; Vracar, L. M.; Krstajic, N. V. Nb-TiO2supported Platinum Nanocatalyst for Oxygen Reduction Reaction in Alkaline

Solutions. *Electrochim. Acta* **2011**, *56* (25), 9020–9026. https://doi.org/10.1016/j.electacta.2011.04.075.

(52) Li, L.; Wei, Z.; Zhang, Y.; Qi, X.; Xia, M.; Zhang, J.; Shao, Z.; Sun, C. DFT Study of Difference Caused by Catalyst Supports in Pt and Pd Catalysis of Oxygen Reduction Reaction. *Sci. China Ser. B Chem.* **2009**, *52* (5), 571–578. https://doi.org/10.1007/s11426-009-0006-2.

(53) Huang, K.; Sasaki, K.; Adzic, R. R.; Xing, Y. Increasing Pt Oxygen Reduction Reaction Activity and Durability with a Carbon-Doped TiO2 Nanocoating Catalyst Support. *J. Mater. Chem.* **2012**, *22* (33), 16824. https://doi.org/10.1039/c2jm32234j.

(54) Shanmugam, S.; Gedanken, A. Carbon-Coated Anatase TiO2 Nanocomposite as a High-Performance Electrocatalyst Support. *Small* **2007**, *3* (7), 1189–1193. https://doi.org/10.1002/smll.200600636.

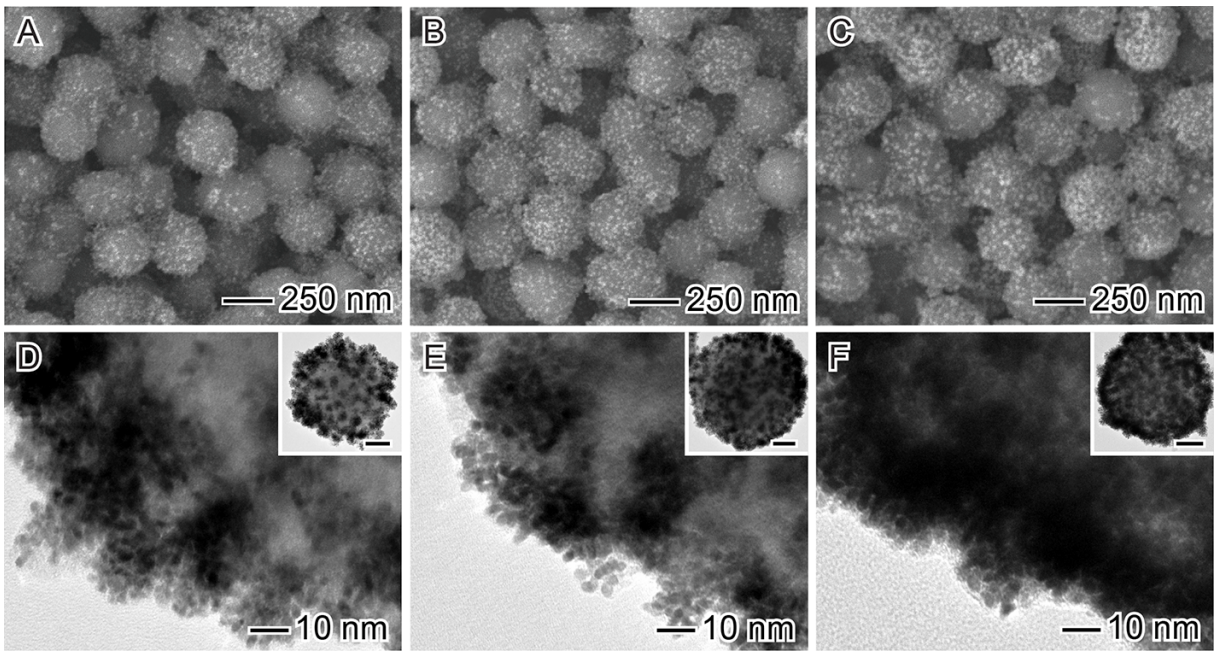

Figure 1. SEM (A-C) and TEM (D-F) images of Pt NPs supported at the surface of TiO_2 colloidal spheres (Pt/TiO_2) after one (A, D), two (B, E), and three (C, F) deposition steps. The scale bars in the insets correspond to 50 nm.

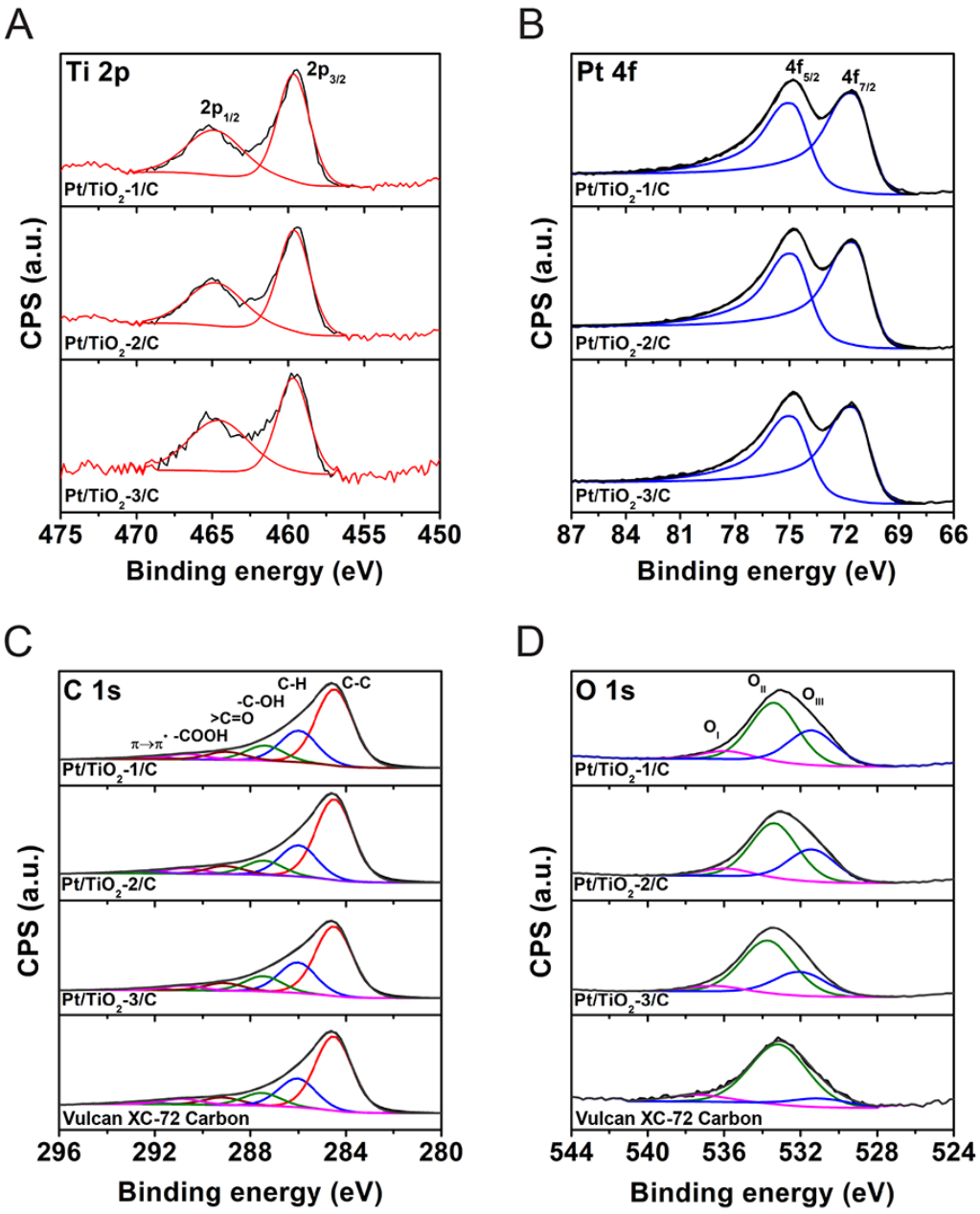

Figure 2. Deconvoluted X-ray photoelectron spectra (XPS) of the Ti 2p (A), Pt 4f (B), C 1s (C), and O 1s (D) core levels for Pt/TiO_2-1/C, Pt/TiO_2-2/C, Pt/TiO_2-3/C, Vulcan XC-72 carbon (top to bottom traces, respectively).

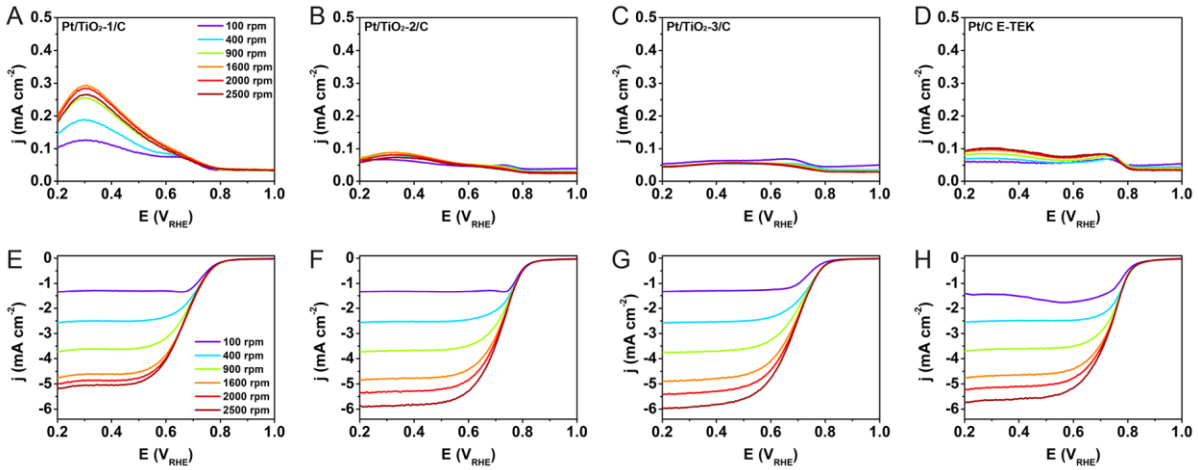

Figure 3. Rotating ring (A-D) and rotating disk (E-H) voltammograms for the ORR employing Pt/TiO_2-1/C (A, E), Pt/TiO_2-2/C (B, F), Pt/TiO_2-3/C (C, G), and Pt/C E-TEK (D, H) as electrocatalysts. These experiments were performed in O_2 saturated 0.5 mol L^{-1} H_2SO_4 with a sweep rate of 10 mVs^{-1} at different rotation rates (as indicated in the insets) and 273 K.

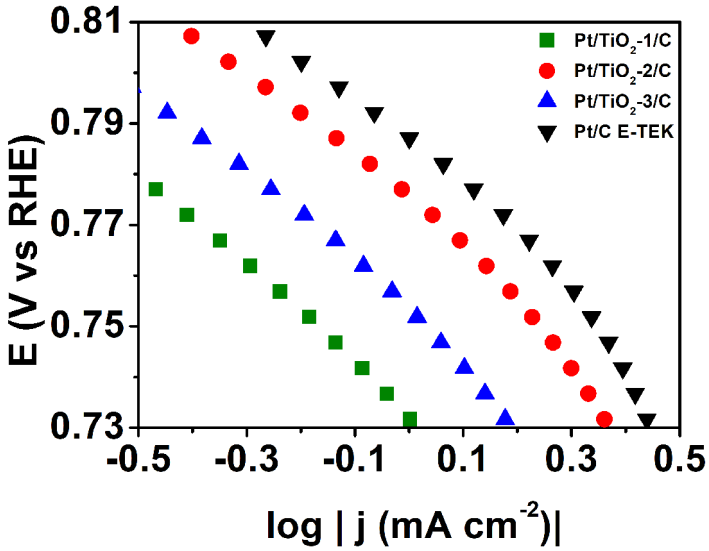

Figure 4. Tafel plots for Pt/TiO_2-1/C (green trace), Pt/TiO_2-2/C (red trace), Pt/TiO_2-3/C (blue trace) and Pt/C E-TEK (black trace). The data was normalized by the geometric area of the electrode and calculated from their corresponding rotating disk electrode values at 1600 rpm.

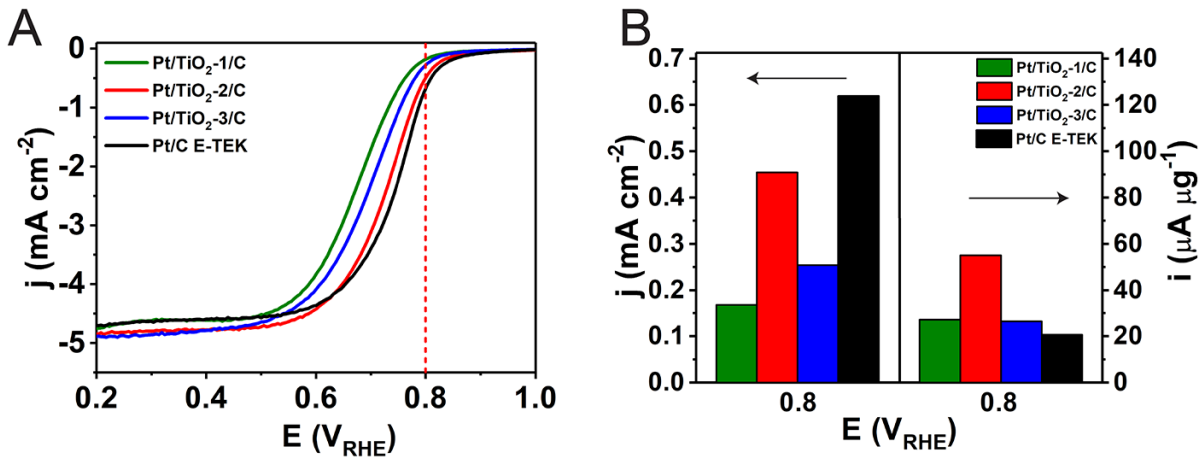

Figure 5. (A) Comparison of rotating disk linear scanning voltammetry for the ORR employing Pt/TiO_2-1/C (green trace), Pt/TiO_2-2/C (red trace), Pt/TiO_2-3/C (blue trace) and Pt/C E-TEK (black trace) as electrocatalysts. The ORR was measured in O_2 saturated 0.5 mol L^{-1} H_2SO_4 solution at a rotation rate of 1600 rpm and T = 273 K. (B) Left panel: current densities at 0.8 V vs RHE for the materials shown in (A); Right panel: current densities divided by the Pt mass at 0.8 V vs RHE for the materials shown in (A).

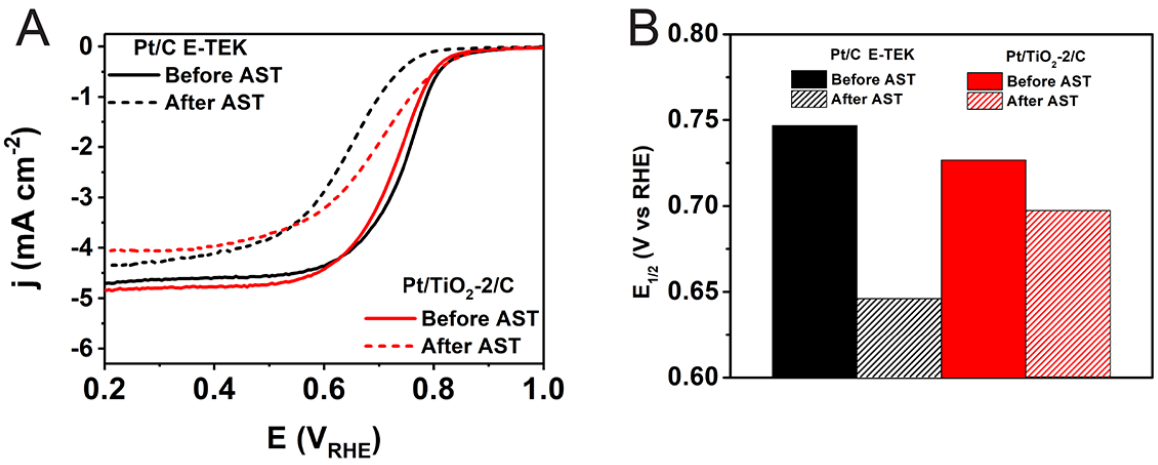

Figure 6. (A) Comparison of ORR polarization curves for Pt/TiO_2-2/C (red trace) and Pt/C E-TEK (black trace) before (solid line) and after (dashed line) accelerated stress tests. The AST were performed using a 100 mV s^{-1} scanning rate and 1000 voltammetric cycles from 0.01 to 1.01 V vs RHE. ORR was performed in O_2 saturated 0.5 mol L^{-1} H_2SO_4 solution at a rotation rate of 1600 rpm. (B) Half-wave potential for each sample before and after the accelerated stress test. T = 273K.

Table 1. Binding energies and surface percentages measured by XPS.

Material	Binding energy (eV)				
	Pt $4f_{7/2}$	Ti $2p_{3/2}$	O 1s		
			O_I	O_{II}	O_{III}
Vulcan XC-72	n.d.	n.d.	530.9 (11)*	533.2 (80)	536.8 (9)
Pt/TiO_2-1/C	71.5	459.6	531.4 (34)	533.4 (58)	536.0 (8)
Pt/TiO_2-2/C	71.5	459.6	531.4 (32)	533.3 (60)	535.9 (8)
Pt/TiO_2-3/C	71.5	459.7	531.7 (28)	533.7 (65)	536.5 (7)

*Species surface percentage

Table 2. Binding energies, surface percentages, and oxygenated carbon/carbon ratios measured by XPS.

Material	Binding energy C 1s (eV)						Intensity (%)
	Peak I C-C	Peak II C-H (defects)	Peak III -C-OH	Peak IV >C=O	Peak V -COOH	Peak VI π→π*	I_{Oxy}/I_C**
Vulcan XC-72	284.5 (57)*	286.0 (21)	287.5 (10)	289.2 (6)	290.8 (4)	292.8 (2)	19
Pt/TiO_2-1/C	284.5 (55)	286.0 (23)	287.4 (10)	289.0 (6)	290.6 (4)	292.4 (2)	26
Pt/TiO_2-2/C	284.5 (57)	286.0 (22)	287.4 (10)	289.0 (6)	290.8 (4)	292.5 (1)	25
Pt/TiO_2-3/C	284.5 (54)	286.0 (24)	287.5 (11)	289.1 (6)	290.8 (4)	292.5 (1)	27

* Species surface percentage

**Intensity of three oxygen-containing functional groups (peaks III-V) in % of total C 1s area.

Table 3. Summary of the RRDE data obtained for the ORR employing Pt/TiO_2-1/C, Pt/TiO_2-2/C, Pt/TiO_2-3/C, and Pt/C-ETEK as electrocatalysts. *n* refers to the number of exchanged electrons and *p* the water proportion efficiency based on the ring and disk currents.[47]

E vs RHE	Pt/TiO_2-1/C		Pt/TiO_2-2/C		Pt/TiO_2-3/C		Pt/C-ETEK	
	n	*p*(H_2O) %	*n*	*p*(H_2O) %	*n*	*p*(H_2O) %	*n*	*p*(H_2O) %
0.60	3.94	97.1	3.98	98.8	3.97	98.3	3.97	98.6
0.50	3.93	96.4	3.97	98.6	3.97	98.3	3.97	98.7
0.40	3.90	94.9	3.97	98.3	3.96	98.1	3.98	98.8
0.30	3.87	93.7	3.96	98.2	3.96	97.9	3.98	99.0
0.20	3.92	95.8	3.97	98.5	3.96	98.0	3.98	99.0
Mean	3.91	95.6	3.97	98.5	3.96	98.1	3.98	98.8

Table of Contents